The Astronomical Journal, 166:26 (11pp), 2023 July https://doi.org/10.3847/1538-3881/acd762

Point Source *C*-band Mueller Matrices for the Green Bank Telescope

Paul Fallon[1], Derck P. Smits[2], Tapasi Ghosh[3], Christopher J. Salter[3,4], and Pedro Salas[3]
[1] Centre for Space Research, North-West University, Private Bag X1290, Potchefstroom 2520, South Africa; paulfallon@telkomsa.net
[2] Department of Mathematical Sciences, University of South Africa, Private Bag X6, Florida 1709, South Africa
[3] Green Bank Observatory, 155 Observatory Road, Green Bank, WV 24915, USA
[4] Emeritus Scientist, Arecibo Observatory, HC3 Box 53995, Arecibo, PR 00612, USA
Received 2022 September 9; revised 2023 May 8; accepted 2023 May 19; published 2023 June 23

Abstract

C-band Mueller matrices for the Green Bank Telescope are presented here which enable on-sky Stokes parameters for point sources at the beam center to be determined. Standard calibrators, 3C 138 and 3C 286, were observed using the Spider program to steer the telescope across a broad range of R.A. on both sides of the zenith transit. For this analysis, only the observations at the peak of the Spider pattern were used rather than the full sweep of the runs. Therefore, the results presented here only apply to point sources at the beam center. The Mueller matrices are shown to vary with frequency and with use of the Hi-Cal or Lo-Cal noise diodes, due to the relative calibration gain between the *X* and *Y* components of the feed. However, the relative calibration gain can be determined from observations of a source with known polarization. Correcting the data for the relative calibration gain prior to data analysis allows for use of a frequency-independent Mueller matrix. This generic Mueller matrix is shown to provide reliable *C*-band polarization measurements.

Unified Astronomy Thesaurus concepts: Astronomical instrumentation (799); Polarimetry (1278); Radio telescopes (1360); Software documentation (1869); Calibration (2179)

1. Introduction

Polarization properties of radio signals provide valuable information about the source, its surrounding region, and the interstellar medium. The versatile Green Bank Telescope (GBT) astronomical spectrometer (VEGAS; Prestage et al. 2015) on the Robert C. Byrd 100 m GBT allows full Stokes measurements to be made, but as with all radio telescopes, instrumental effects distort the observed signal. The feed, telescope structure, dish surface, coaxial cables, optical fibers, and electronics can introduce gain and phase differences in the individual measurement channels which modify the polarization. Measured Stokes values can be corrected using an empirically determined Mueller matrix to obtain the source polarization parameters.

Mueller matrices have been determined previously for the GBT. The *L*-band system was calibrated by Liao et al. (2016) and the C band by Robishaw & Heiles (2006). However, subsequent system changes, e.g., replacement of the *C*-band receiver in 2014, result in the calibrations no longer being valid.

2. Observation

The *C*-band receiver on the GBT contains a single waveguide located at the Gregorian focus of the telescope, feeding into a cooled orthomode transducer (OMT) that produces two orthogonal linearly polarized outputs. The linear *X* component of the feed is aligned parallel to the elevation axis (horizontal) and the *Y* component is aligned perpendicular to the elevation axis (vertical) on the alt-az mounted telecope. Resonances within the bandpass can arise in the OMT, but none are listed for the *C*-band system. There are two noise diodes (NDs) with levels of ∼10% (Lo-Cal) and ∼100% (Hi-Cal) of the system temperature that can be used for flux calibration. The nominal frequency range of the *C*-band system is 3.95–7.8 GHz. Further details regarding the receiver system can be found in the GBT Observers Guide v4.0.[5]

The VEGAS spectrometer was used for all our observations; it consists of eight independent spectrometers (banks) that can be used simultaneously, each one producing a full set of polarization products. The auto- (*XX* and *YY*) and cross-correlation (*XY* and *YX*) terms produced by the VEGAS spectrometer were calibrated as described in Section 3 and Appendix A, and then used to obtain the observed Stokes parameters, which are defined as

$$I_{\rm obs} = XX + YY \quad (1)$$

$$Q_{\rm obs} = XX - YY \quad (2)$$

$$U_{\rm obs} = 2 * XY \quad (3)$$

$$V_{\rm obs} = 2 * YX. \quad (4)$$

The convention used here is that the polarization angle is measured east of north, as specified by IAU Commissions 25 and 40. The Stokes *V* component uses the standard IAU definition for the circular component in radio astronomy (IEEE 2018), i.e., $V = \mathrm{RCP} - \mathrm{LCP}$. The double reflection produced by the main dish and the subreflector ensures that the Stokes *V* component from the correlator matches that of the incoming signal. When comparing results from other telescopes, it is important to check what definitions have been used for the Stokes parameters (Robishaw & Heiles 2021).

The Mueller matrix measurements comprised observing linearly polarized point sources over a range of parallactic angles (PAs) on both sides of the prime meridian. To accomplish this the GBT Spider scan routine was used. It consists of four scans centered on-source, starting and ending three beam widths off center. The on-sky trajectory of the Spider scan is shown in Figure D.1 on page 213 of the GBT Observers Guide v4.0. The Hi-Cal ND was fired for 10 s (with

[5] Available at https://www.gb.nrao.edu/scienceDocs/GBTog.pdf.

1 s switching period) before and after each run along a leg of the Spider scan. The Spider routine acquired 80 observations of 1 s duration each along each leg. Observation 40 was the on-source measurement that had the maximum flux reading along each leg. Each full Spider procedure lasted ∼14 minutes.

The Spider run configuration comprised, the eight banks of the spectrometer using VEGAS mode 4, each covering a bandwidth of 187.5 MHz with central frequencies evenly distributed from 4.3 to 7.1 GHz (see Table 1). Only data from the middle 1/3 of the bandwidth ($\Delta\nu \sim 60$ MHz) were used for the analysis. Two linearly polarized calibration sources were measured. 3C 286 was observed for 3 hr on 2021 January 2 and 3C 138 for 6 hr on 2021 January 13.

Spectral line frequency-switched observations using VEGAS mode 15 and the Lo-Cal ND (with 1 s switching period) were made on 2021 January 5 and 2021 November 27. The eight banks of the VEGAS spectrometer were centered on frequencies of $\nu = 4.765$, 4.751, 4.660, 4.830, 6.033, 6.049, 6.181, and 6.668 GHz, each with a bandwidth of 11.72 MHz, but only the middle 1/3 of the data was used, giving $\Delta\nu \sim 4$ MHz. On 2021 January 5, 3C 138 was observed before our target source for 210 s to calibrate the polarization and the source B0529+075 for 6 minutes to calibrate the flux. On the November run, 3C 138 and B0529+075 were observed (for 120 s and 180 s, respectively) using both the above spectral line and the evenly spaced Spider run frequency settings before our source observation, and 3C 138 was observed again with both frequency settings after our source observations. All observations were part of project *AGBT20B_424*.

3. Analysis

Analysis of the auto-correlation terms is straightforward and can be accomplished using standard GBTIDL routines such as *getfs* and *getps*, whereas the cross-correlation terms need to be reduced using polar coordinates. Data calibration is achieved using the ND-on and ND-off modes of either the Hi-Cal or Lo-Cal ND. The *XX* and *YY* spectra are each calibrated separately, whereas the *XY* and *YX* spectra are calibrated simultaneously in polar coordinates as described in Appendix A. For these reductions the same $T_{\rm cal}$ calibration constant has been used for all four components as explained in Section 4.3 and Appendix A. A new set of GBTIDL analysis routines has been developed to perform the reductions (Fallon 2022). These routines have been rigorously tested and shown to produce the same calibrated outcomes as the standard routines for the auto-correlation terms. Observed Stokes parameters were determined from the calibrated spectra for each spectrometer bank using Equations (1)–(4).

Because the GBT has an alt-azimuth mount, the PA of the feed rotates on the sky. The observed parameters are rotated from the sky frame by the rotation matrix $\boldsymbol{M}_{\rm sky}$ and then distorted further by instrumental effects that are described in terms of the Mueller matrix $\boldsymbol{M}_{\rm Mueller}$. The observed Stokes values are a product of the Mueller matrix, the rotation matrix and the source Stokes parameters, i.e.,

$$\begin{bmatrix} I_{\rm obs} \\ Q_{\rm obs} \\ U_{\rm obs} \\ V_{\rm obs} \end{bmatrix} = \boldsymbol{M}_{\rm Mueller} \cdot \boldsymbol{M}_{\rm sky} \begin{bmatrix} I_{\rm src} \\ Q_{\rm src} \\ U_{\rm src} \\ V_{\rm src} \end{bmatrix}. \quad (5)$$

Once the appropriate Mueller matrix is determined, source Stokes parameters can be obtained from the inverse of Equation (5),

$$\begin{aligned} \begin{bmatrix} I_{\rm src} \\ Q_{\rm src} \\ U_{\rm src} \\ V_{\rm src} \end{bmatrix} &= (\boldsymbol{M}_{\rm Mueller} \cdot \boldsymbol{M}_{\rm sky})^{-1} \begin{bmatrix} I_{\rm obs} \\ Q_{\rm obs} \\ U_{\rm obs} \\ V_{\rm obs} \end{bmatrix} \\ &= (\boldsymbol{M}_{\rm sky})^{-1} \cdot (\boldsymbol{M}_{\rm Mueller})^{-1} \begin{bmatrix} I_{\rm obs} \\ Q_{\rm obs} \\ U_{\rm obs} \\ V_{\rm obs} \end{bmatrix}. \end{aligned} \quad (6)$$

The theory used to determine single dish Mueller matrices has been described by Heiles et al. (2001), Heiles (2002), and Robishaw & Heiles (2021). These equations are presented in Appendix B where it can be seen that the observed fractional Stokes parameters are functions of the PA, the fractional source Stokes parameters, and the five Mueller matrix parameters. The observed fractional Stokes parameters from the Spider runs were fitted to Equations (B6)–(B8) using the Add-in Solver in Excel.[6] The starting values for the fitting routine used the values for the Mueller matrices presented in Robishaw & Heiles (2006). To check that the routine is finding an absolute rather than a local minimum, tests were done with a wide range of starting values. In all cases the iteration returned the same final values. The final values are the five Mueller matrix parameters and the source parameters $(Q/I,\ U/I)_{\rm src}$. In Appendix B it is pointed out that we assume $V_{\rm src} = 0$, however the fitting process can be conducted without using this constraint.

Mueller matrices are derived from our Spider scan observations, which covered a wide range of PAs. Fewer observations can be used to determine Mueller matrices (but this might increase the uncertainties in the values), provided at least two observations are made at different PAs and the observed fractional Stokes values outnumber the number of unknowns in Equations (B5)–(B8). Observations of 3C 138 in 2021 November were made at two PAs (before and after our spectral line source observations) using the Lo-Cal ND to calibrate the spectra. Fitting Equations (B5)–(B8) to the observations and using values of $(Q/I,\ U/I)_{\rm src}$ determined from the Spider runs, provided sufficient constraints for the Mueller matrix parameters to be uniquely determined using Solver, but with higher uncertainty than for the Spider runs.

4. Determining the Mueller Matrix

The observed fractional Stokes parameters as a function of PA for the Spider run on 3C 286 are shown in Figure 1 and for 3C 138 in Figure 2. The Mueller and rotation matrix equations fitted to the observed values are shown as solid lines in Figures 1 and 2. The middle *C*-band frequencies display better quality fits than the outside frequencies; the most data scatter was observed in the 7.1 GHz band.

Application of the derived Mueller matrices using, Equation (6), to the observed data in Figures 1 and 2 gives the source Stokes parameters presented in Figure 3. The calculated source values show no statistically significant variation with PA. The source Stokes parameters determined in this manner for all the observed frequencies are presented in Figure 4, and show slight variation with frequency.

[6] https://support.microsoft.com/en-us/office/load-the-solver-add-in-in-excel-612926fc-d53b-46b4-872c-e24772f078ca

Table 1
GBT Spider Run Mueller Matrices for Each of the Eight Observed *C*-band Frequencies

4.300 *GHz*

$$\begin{bmatrix} 1.0000(0) & 0.0440(25) & -0.0010(4) & -0.0052(4) \\ -0.0441(25) & -1.0000(0) & 0.0000(0) & 0.0068(23) \\ 0.0015(4) & -0.0007(3) & -0.9941(2) & -0.1082(22) \\ -0.0048(2) & 0.0068(23) & -0.1082(22) & 0.9941(3) \end{bmatrix}$$

4.700 *GHz*

$$\begin{bmatrix} 1.0000(0) & -0.0009(35) & 0.0020(14) & -0.0007(0) \\ 0.0009(35) & -1.0000(0) & 0.0000(0) & -0.0004(1) \\ -0.0019(14) & 0.0000(0) & -0.9946(3) & -0.1042(28) \\ -0.0009(1) & -0.0004(1) & -0.1042(28) & 0.9946(3) \end{bmatrix}$$

5.100 *GHz*

$$\begin{bmatrix} 1.0000(0) & 0.0003(25) & 0.0056(7) & -0.0005(2) \\ -0.0003(25) & -1.0000(0) & 0.0000(0) & 0.0085(31) \\ -0.0055(7) & -0.0008(3) & -0.9960(3) & -0.0888(31) \\ -0.0010(1) & 0.0084(30) & -0.0888(31) & 0.9960(3) \end{bmatrix}$$

5.500 *GHz*

$$\begin{bmatrix} 1.0000(0) & 0.0189(27) & -0.0003(8) & 0.0000(2) \\ -0.0189(26) & -0.9999(0) & 0.0000(0) & 0.0136(5) \\ 0.0003(8) & -0.0011(0) & -0.9966(1) & -0.0821(14) \\ 0.0003(3) & 0.0136(5) & -0.0821(14) & 0.9965(1) \end{bmatrix}$$

5.900 *GHz*

$$\begin{bmatrix} 1.0000(0) & -0.0289(44) & -0.0035(2) & 0.0002(9) \\ 0.0289(44) & -0.9997(3) & 0.0000(0) & 0.0172(178) \\ 0.0035(3) & -0.0013(14) & -0.9973(2) & -0.0729(33) \\ 0.0000(13) & 0.0171(178) & -0.0729(34) & 0.9970(6) \end{bmatrix}$$

6.300 *GHz*

$$\begin{bmatrix} 1.0000(0) & -0.0231(16) & -0.0008(2) & -0.0035(3) \\ 0.0231(18) & -0.9982(1) & 0.0000(0) & -0.0017(596) \\ 0.0012(3) & 0.0005(59) & -0.9950(5) & -0.0992(51) \\ -0.0033(11) & -0.0016(593) & -0.0994(51) & 0.9933(6) \end{bmatrix}$$

6.700 *GHz*

$$\begin{bmatrix} 1.0000(0) & 0.0386(76) & -0.0049(33) & 0.0040(20) \\ -0.0385(77) & -0.9991(9) & 0.0000(0) & 0.0240(361) \\ 0.0048(34) & -0.0014(18) & -0.9991(5) & -0.0406(119) \\ 0.0048(9) & 0.0240(361) & -0.0406(119) & 0.9982(14) \end{bmatrix}$$

7.100 *GHz*

$$\begin{bmatrix} 1.0000(0) & -0.0181(21) & 0.0028(47) & -0.0036(5) \\ 0.0182(19) & -0.9993(7) & 0.0000(0) & -0.0230(283) \\ -0.0027(46) & 0.0000(2) & -0.9996(4) & -0.0215(170) \\ -0.0033(1) & -0.0230(283) & -0.0215(170) & 0.9990(3) \end{bmatrix}$$

Note. For each component of the Mueller matrix, uncertainties for the least significant figures are in parentheses.

The average linear polarization, determined from the source Stokes values over the eight frequencies, for 3C 286 is $11.5\% \pm 0.1\%$ at an angle of $32.5° \pm 0.1°$, and for 3C 138 it is $10.39\% \pm 0.09\%$ at an angle of $-11.4° \pm 0.2°$. These match the listed polarizations of 3C 286 and 3C 138 at these frequencies on the NRAO website.[7] One of the beauties of this method to determine the Mueller matrix is that it makes no assumptions about the source polarization parameters and thus provides an independent measure of their values.

The small variation of source Stokes values with frequency can be used to show the frequency dependence of the source polarization. The polarization angle and linear polarization percentage as functions of frequency for 3C 286 and 3C 138 are shown in Figures 5(a) and (b) respectively. As can be seen from the plots, the polarization of 3C 286 suggests a *C*-band frequency dependence, whereas 3C 138 shows no clear frequency dependent pattern across the *C*-band—these frequency dependencies of the polarization parameters are consistent with the spread of values on the NRAO website (see footnote 7).

The Mueller matrices determined from the Spider runs are presented in Table 1. The values are the average for the separate observations of 3C 286 and 3C 138 and the uncertainty is the standard error of the mean. The matrices have diagonal terms close to ± 1 and relatively small off-diagonal terms.

The results presented here only use data from when the source was at the center of the beam (i.e., when the signal was at maximum), and when the beam was pointed off-source (to determine the background signal level). The rest of the Spider scan data can be used to determine the polarization parameters across the whole beam of the telescope. Analysis of the half-power points averaged over all the Spider scan data produces Mueller matrices similar to the beam-center results. Further analysis of the off-axis signal data has not been attempted here.

4.1. Frequency Dependence of the Mueller Matrix Parameters

In Figures 6(a)–(e), the five Mueller matrix parameters derived in determining the matrices in Tables 1, 2 and 3 are presented as functions of frequency.

The ΔG parameter is the relative calibration gain difference between the *X* and *Y* components of the feed and is the basis of the m_{IQ} and m_{QI} Mueller matrix terms (see Appendix B). It has a dominant impact when applying the Mueller matrix to observations of sources with partial linear polarization, in particular when Stokes *Q* is substantially smaller than Stokes *I*. The ΔG values obtained from our observations differ between the Hi-Cal and Lo-Cal NDs, as seen in Figure 6, resulting in different Mueller matrices required for the two NDs, as described in Section 4.2.

In addition, the ΔG values do not show any analytically predictable frequency dependence across the range of the new *C*-band receiver, although such a variation was reported for the old GBT *C*-band receiver (Heiles et al. 2003). Because the Mueller matrix is sensitive to the value of ΔG, using slightly different ΔG values with differences less than the dispersion seen in Figure 6 results in inaccurate polarization values. Interpolating values of ΔG for specific transition frequencies using values from the matrices in Table 2 results in polarization angle error spread of $\pm 8°$ and a linear polarization fraction dispersion of $\pm 2\%$. The polarization results from a linear fit of ΔG with frequency show an even broader dispersion. Subsequent separate Spider observations (T. Robishaw 2023, private communication) for 64 different *C*-band frequencies displayed similar ΔG values and frequency dependence confirming the ΔG frequency behavior as real and not just measurement uncertainty.

The ψ parameter changes with frequency, as shown in Figure 6(b). Because ψ is the phase difference between the calibration ND signal and the incoming radiation (Appendix B), a linear frequency dependence is expected due

[7] https://science.nrao.edu/facilities/vla/docs/manuals/obsguide/modes/pol (Table 7.2.7), and https://science.nrao.edu/facilities/vla/docs/manuals/obsguide/modes/flux-density-scale-polarization-leakage-polarization-angle-tables.

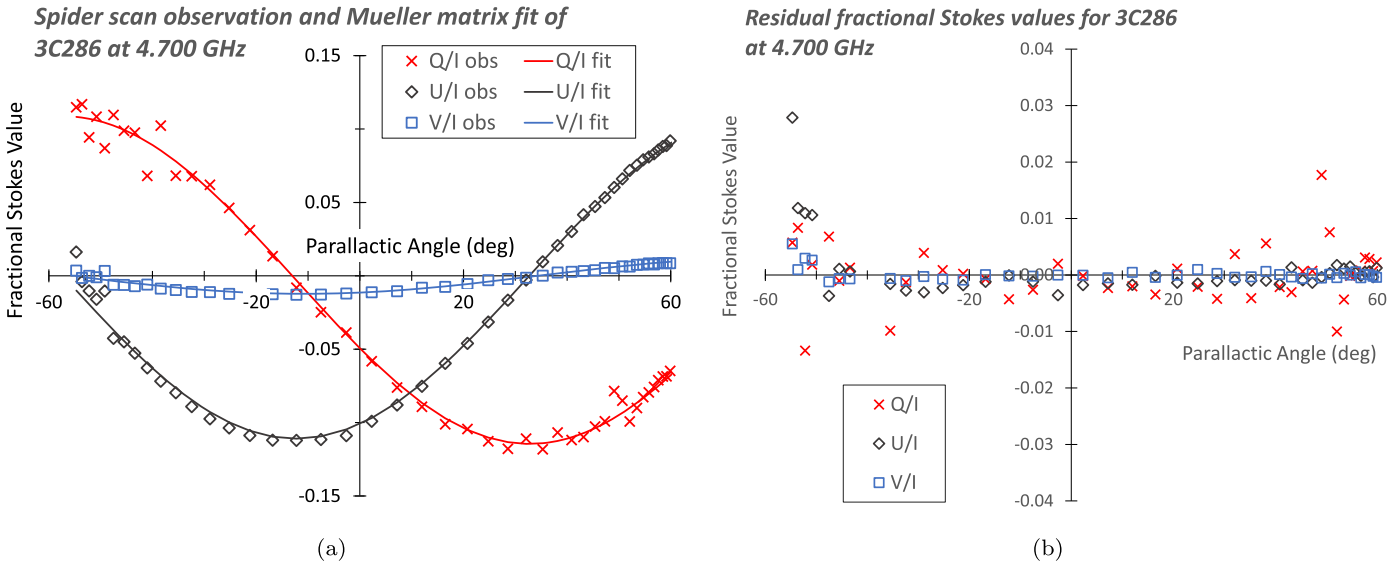

Figure 1. (a) Observed 3C 286 fractional Stokes parameters as a function of PA fitted with Mueller matrix equations. (b) Differences between the observed and fitted fractional Stokes parameters, indicating no systematic variation.

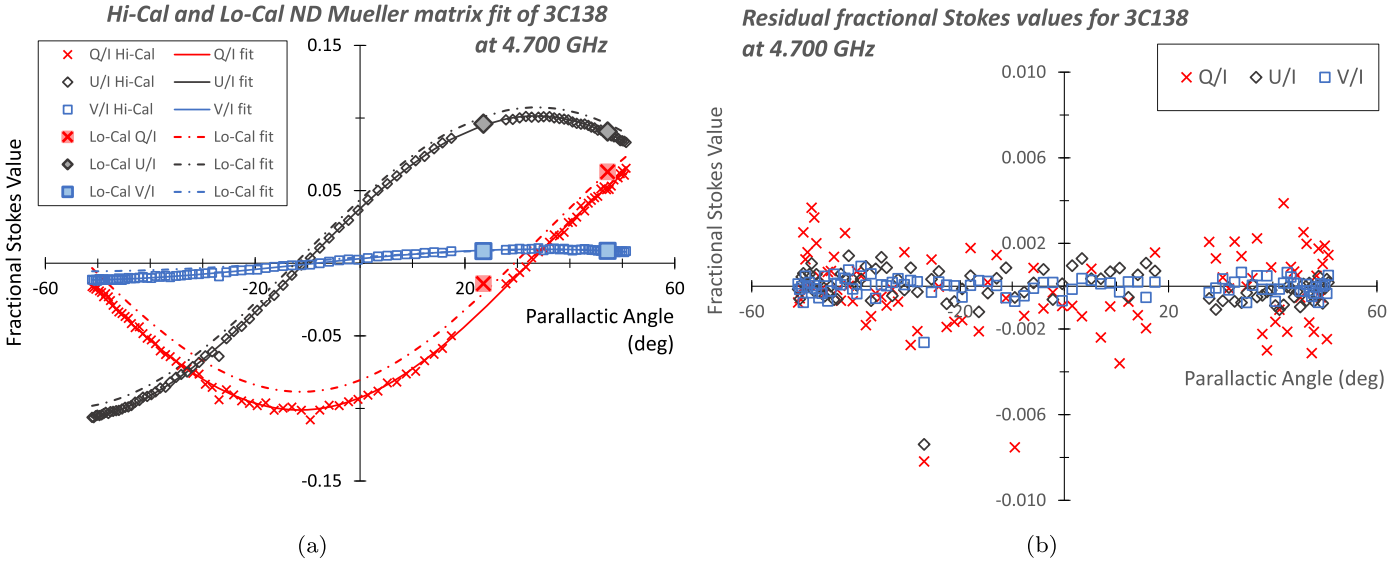

Figure 2. (a) Observed 3C 138 fractional Stokes parameters as a function of PA, fitted with Mueller matrix equations using solid line. The Lo-Cal ND observations are shown with larger symbols and dotted–dashed lines, and indicate a difference with the Hi-Cal ND results. Because all the Lo-Cal Q/I, U/I and V/I parameters are fitted simultaneously, the Lo-Cal Q/I and U/I values are offset from the calculated curve. (b) Differences between the observed and fitted fractional Stokes parameters for the Hi-Cal ND data points, indicating no systematic variation. The vertical scale is different to that in Figure 1(b) which has more scatter.

to path length differences. The ψ frequency derivative, from the linear fit in Figure 6(b), implies a difference of about 1 mm between the calibration ND signal and the incoming radiation, which is reasonable for the components involved. The Hi-Cal and Lo-Cal ND data have slightly different slopes, but this difference is not statistically significant.

From Figure 6(c), it can be seen that the 2α parameter scatters around 180°, with increasing dispersion at the high frequency end of the C band. However, it does not appear to have a frequency dependence. Heiles et al. (2003) presents values for α over a range of frequencies which show no change across the C band, but differences between the L, C, and X band. The ϵ and ϕ parameters, shown in Figures 6(d) and (e), have a small impact on the C-band Mueller matrices. They scatter around values of 0 and 0°, respectively. Any inaccuracy in ΔG or ψ will result in additional noise or scatter in the fitted outcome for α, ϵ, and ϕ.

4.2. Hi-Cal and Lo-Cal ND Mueller Matrix Differences

The Mueller matrix determined from our observations, differs depending on whether the Hi-Cal or Lo-Cal ND is used to calibrate the data. Initial analysis applying the Hi-Cal Mueller matrix to observations of 3C 138 made using the Lo-Cal ND on 2021 January 5 produced inaccurate polarization outcomes. Another set of observations made using the Lo-Cal ND in 2021 November produced results similar to the January set, creating the realization that different Mueller matrices are required for observations with the Lo-Cal or Hi-Cal ND. This led to derivation of the Lo-Cal ND Mueller matrix from observations of 3C 138 at different PAs. Because the fractional source Stokes parameters for 3C 138 are known from the fitting process using the Spider run, these values can be substituted into Equations (B2) and (B3) so that Equations (B5)–(B8) contain only the five unknown parameters of the Mueller matrix. Observations of the polarization calibrator made before

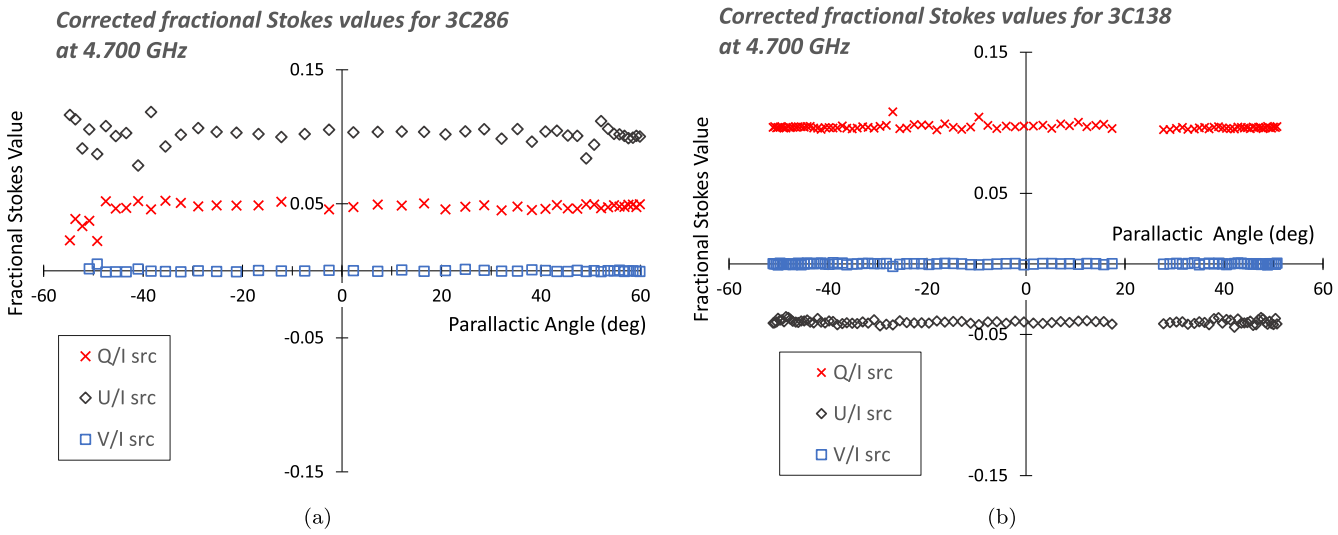

Figure 3. Source Stokes parameters for (a) 3C 286 and (b) 3C 138 calculated by applying Equation (6) to the observed values in Figures 1 and 2. The 3C 286 data shows some noise at PAs above and below 40°, this noise is seen in the observed fractional Stokes parameters in Figure 1.

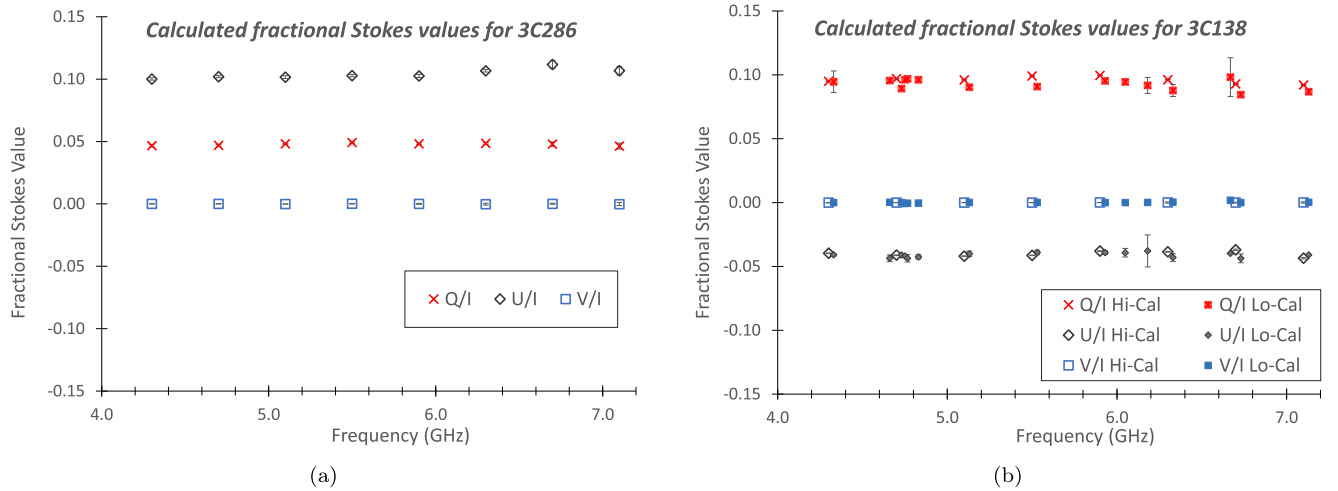

Figure 4. Source Stokes parameters for (a) 3C 286 and (b) 3C 138 for the observed *C*-band frequencies. The points are average values from the frequency set of Spider scans. The error bars are the standard error of the mean and, for the Spider scan (Hi-Cal ND) data, are smaller than the plotted symbols; because the top and bottom of the error bar are almost on top of one another in some cases, the error bar appears as a single horizontal line. Figure (b) includes values from the Lo-Cal ND calibrator observations. Note that the Lo-Cal data points for the evenly spaced frequencies have been offset to the right by 30 MHz so that they do not lie on top of the Hi-Cal points.

and after our program source have different PAs and can be fitted to these equations to derive the Mueller matrix parameters. In Figure 2 the Lo-Cal ND observations, shown with larger symbols and dotted–dashed lines, are at PAs of 23.5° and 47.2°. Fractional Stokes Q/I and U/I show a difference between Hi-Cal and Lo-Cal ND observations, highlighting the need for different Mueller matrices depending on which ND is used.

Mueller matrices determined for Lo-Cal ND observations using the above method are presented in Table 2 in Appendix B for evenly spaced frequencies and in Table 3 for the maser frequencies used in our program observations. There are differences between the Hi-Cal and Lo-Cal ND Mueller matrices parameters but the differences are not significant at all the observed frequencies. The differences, an example of which is shown in Table 4 for observations at 4.700 GHz, are mainly due to the ΔG parameter.

4.3. Calibration of the GBT Polarization Products

The GBT provides calibration values for the four polarization products *XX*, *YY*, *XY*, and *YX*, with seperate $T_{\rm cal}$ values stored and included in the spectrum SDFITS header (Appendix A). The standard GBT calibration provides the same $T_{\rm cal}$ value for *XX*, *XY*, and *YX* and a different value for *YY*. These values are calibrated from on sky observations and vary with frequency. However, as noted by Goddy et al. (2020), these values have not been regulary updated and are only expected to be accurate at the 15%–20% level.

Using the different *XX* and *YY* $T_{\rm cal}$ calibrations provided in the spectrum SDFITS header resulted in larger Mueller matrix ΔG values than if the same $T_{\rm cal}$ value was used for all the polarization products. In addition, the ΔG difference between the Hi-Cal and Lo-Cal ND Mueller matrices is exacerbated. As a result, all the analysis in this paper has been done using the same $T_{\rm cal}$ value for all four polarization products, and thus use

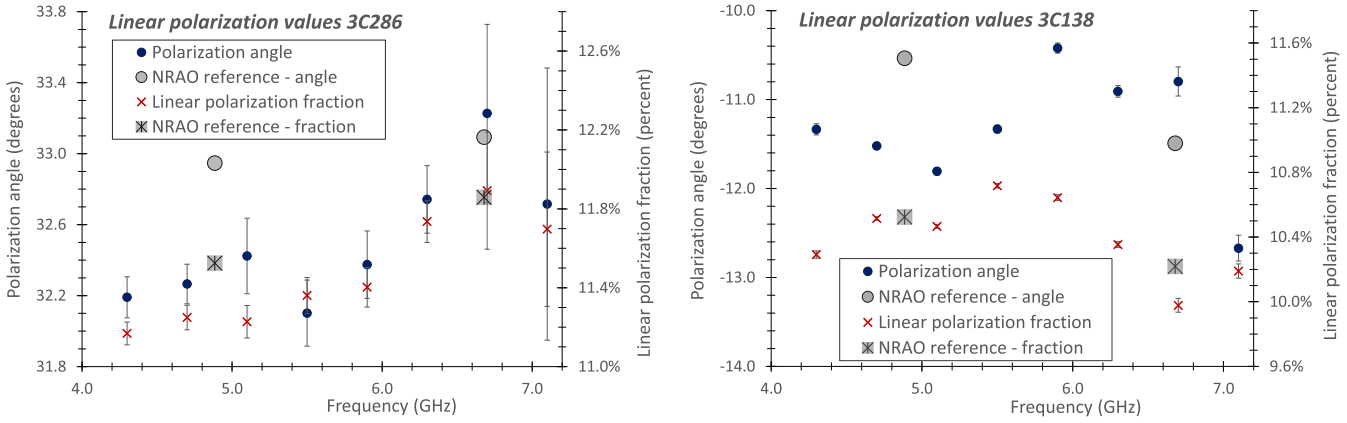

(a) (b)

Figure 5. Polarization values as a function of frequency for (a) 3C 286 and (b) 3C 138. The points are average values and the error bars are the standard error of the mean from all the Spider scan observations, using Equation (6) to obtain source Stokes parameters. The NRAO reference values are the current polarization values on the NRAO website (see footnote 7).

of the Mueller matrices presented in Tables 1–4 only apply to spectra calibrated in the same manner.

In the next section, a method is described to modify ΔG to adjust for inaccuracy in the relative *XX* and *YY* $T_{\rm cal}$ calibration, so that a generic, frequency-independent Mueller matrix can be utilized.

5. Frequency-independent Mueller Matrix

If ΔG can be determined independently then the spectra can be corrected for the relative calibration gain prior to determination and use of the Mueller matrix. This correction removes the unpredictable ΔG change across the *C* band and does away with the need for bespoke ND and frequency Mueller matrices.

5.1. Independent Calculation of the Relative Calibration Gain

The relative calibration gain is defined as

$$XX_{\rm calibrated,modified} = XX_{\rm calibrated}(1 - \Delta G/2) \quad (7)$$

$$YY_{\rm calibrated,modified} = YY_{\rm calibrated}(1 + \Delta G/2) \quad (8)$$

where $XX_{\rm calibrated}$ and $YY_{\rm calibrated}$ are the calibrated observed spectra while $XX_{\rm calibrated,modified}$ and $YY_{\rm calibrated,modified}$ are the expected polarization spectra should no instrument correction be required (Heiles et al. 2001). These modified spectra, when converted using Equations (1) and (2) into Stokes parameters, describe the sky rotated source signal $I_{\rm src}$ and $Q_{\rm src,rot}$.

From Equations (7) and (8) the relative calibration gain can be expressed as

$$\Delta G/2 = [(Q/I)_{\rm obs} - (Q/I)_{\rm src,rot}]/[1 - (Q/I)_{\rm src,rot}(Q/I)_{\rm obs}]. \quad (9)$$

For a source with known polarization and thus known (*Q*/*I*) and (*U*/*I*), the $(Q/I)_{\rm src,rot}$ can be determined from Equation (B2). Note that the fractional Stokes values can be calculated from the polarization angle and the linear polarization percentage, which are available for all the well-known polarization calibrators. This allows ΔG to be determined from observations of a source with known polarization.

The ΔG values were determined for the Spider scan observations of 3C 286, using the source Stokes parameters presented in Section 4 and applying Equation (9). These ΔG values show no statistically significant variation across the PA observations and the average value (per frequency) is the same as the frequency specific Mueller matrix derived values shown in Figure 6. As discussed in Sections 4.1 and 4.2, the ΔG values do vary with frequency and with use of either the Hi-Cal or Lo-Cal ND.

5.2. Generic GBT Mueller Matrix

Once the ΔG value is determined for a specific set of observing conditions, the observed *XX* and *YY* auto-correlation polarization products can be modified using Equations (7) and (8). Alternatively, rewriting Equation (9) gives

$$(Q/I)_{\rm modified} = (Q/I)_{\rm src,rot} = \frac{1}{1 - (\Delta G/2)(Q/I)_{\rm obs}}[(Q/I)_{\rm obs} - \Delta G/2], \quad (10)$$

allowing the observed fractional Stoke (*Q*/*I*) value to be modified. Mueller matrices fitted to the modified 3C 286 data result in a zero ΔG parameter with the other Mueller matrix parameters unchanged from the values shown in Figures 6(b), (c), (d), and (e). These Mueller matrices are independent of the frequency and ND variability of the ΔG parameter.

The Mueller matrix applicable to the ΔG modified data, can be described by a zero ΔG and the ψ parameter determined from the linear function shown in Figure 6(b). The 2α parameter can be set to 180°, and the ϵ and ϕ parameters to zero, which are reasonable values for these parameters, as seen in Figures 6(c), (d), and (e). The scatter in these parameters has negligible impact on the calculated polarization values. This generic Mueller matrix has the form

$$\boldsymbol{M}_{\rm Generic\ Mueller} = \begin{bmatrix} 1 & 0 & 0 & 0 \\ 0 & -1 & 0 & 0 \\ 0 & 0 & \cos\psi & \sin\psi \\ 0 & 0 & \sin\psi & -\cos\psi \end{bmatrix}, \quad (11)$$

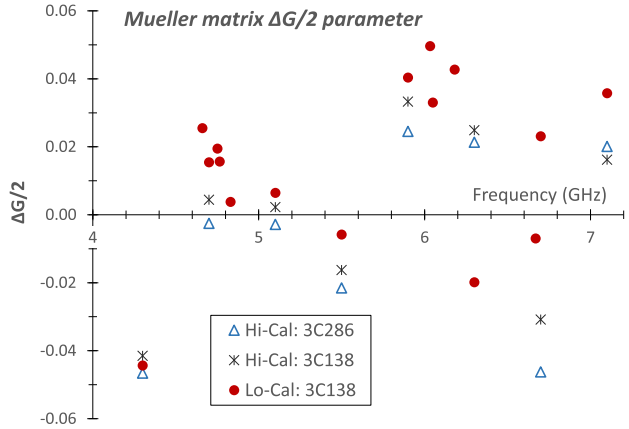

(a)

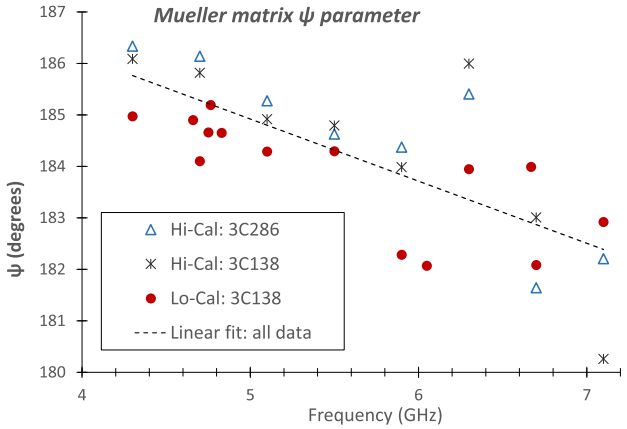

(b)

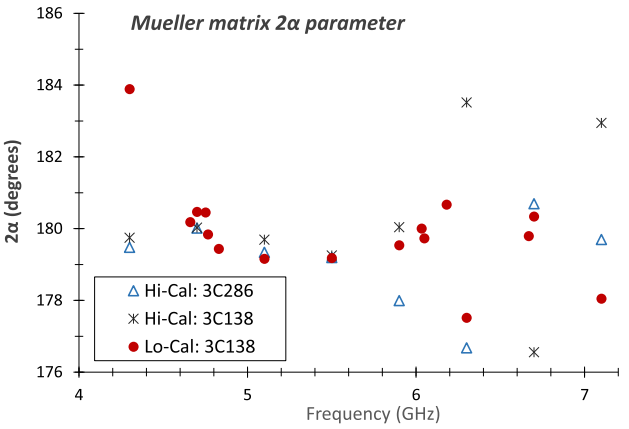

(c)

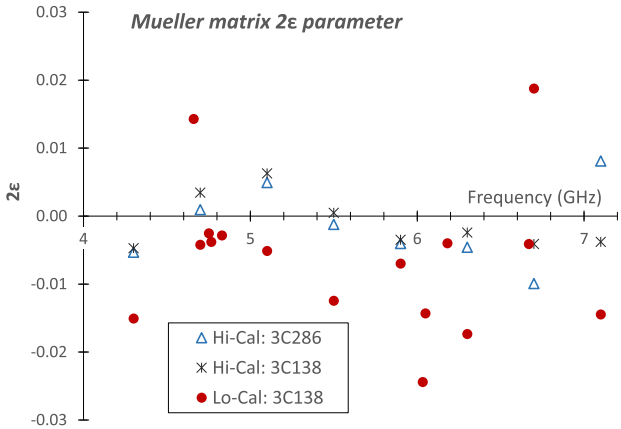

(d)

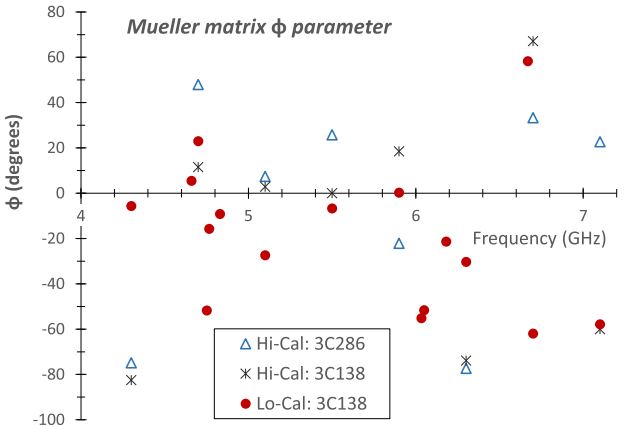

(e)

Figure 6. Mueller matrix parameters as a function of frequency. (a) $\Delta G/2$, (b) ψ, with a linear best fit through all the data points. The linear fit has values of 190.95 − 1.2067 × Frequency (GHz), (c) 2α, (d) 2ϵ, and (e) ϕ.

where $\psi = 190.95 - 1.2067 \times$ Frequency (GHz). Provided that spectra have been modified for ΔG as described in Section 5.1, this generic Mueller matrix can be applied to determine the polarization of sources whose spectra have been observed with the GBT.

5.3. Testing the Generic GBT Mueller Matrix

This generic Mueller matrix has been applied to the ΔG modified 3C 286 Spider scan data and the resulting polarization values, shown in Figure 7, are closely aligned and generally within the error range of the frequency bespoke Mueller matrix polarization results.

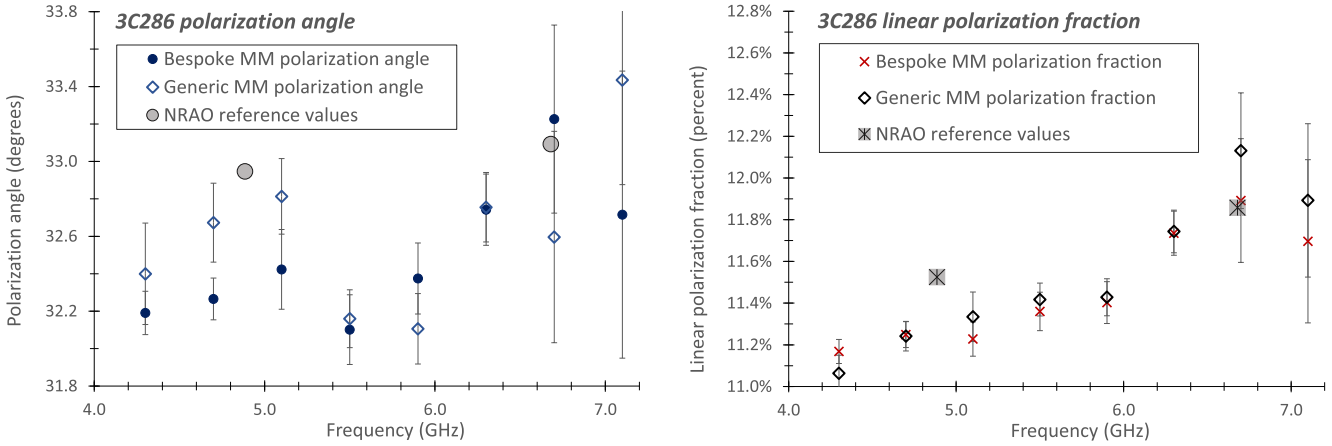

Figure 7. Polarization values for 3C 286 as a function of frequency (a) polarization angle and (b) linear polarization fraction. The graphs compare the frequency bespoke Mueller matrix analysis outcomes shown in Figure 5(a) with the results of using the generic Mueller matrix to determine the polarization.

The 3C 138 Spider scan data has also been tested by determining the ΔG correction, using this to modify the data and applying the generic Mueller matrix to determine the polarization properties. The resulting polarization values are within the range determined by use of the bespoke Mueller matrices described in Section 4 and shown in Figure 5(b). The Lo-Cal ND observation, described in Section 4.2, were tested and the polarization results are within the same range of outcomes calculated using the bespoke Mueller matrices.

This testing shows that the generic Mueller matrix produces reliable polarization results. It is recommended that observations to determine ΔG are done at two or more PAs, as the results improve with the number of different pointings, as evidenced with analysis of the Lo-Cal ND data.

6. Conclusion

In order to measure point-source polarization, *C*-band Mueller matrices have been determined for the GBT. The Hi-Cal ND Mueller matrices are calculated from measurements over a range of PAs and, hence, have lower uncertainties than the Lo-Cal ND measurements that are determined from only two or three pointings.

The Mueller matrices determined using the same calibration for all four polarization products, differ with use of either the Hi-Cal or Lo-Cal ND calibrator and vary with frequency. This is a result of the relative calibration gain or ΔG parameter not changing in a predictable manner with frequency, suggesting a different Mueller matrix calibration is required for each specific observational configuration.

However, observations of a source with known polarization parameters allows for an independent determination of the relative calibration gain. This ΔG value can be used to correct the data prior to analysis. The modified data enables a generic frequency and ND independent Mueller matrix to be used in the calculation of *C*-band polarization. These polarization outcomes are shown to have accuracy similar to the polarization values determined using frequency and ND bespoke Mueller matrices applied to unmodified data. Observations and analysis over an 18 months period indicate Mueller matrix stability on this timescale at the GBT.

The analysis described in this paper could be used to determine Mueller matrices at other frequency bands and at other single dish telescopes.

The authors were provided additional GBT observation sessions for project *AGBT20B_424* in order to determine the Mueller matrices. The support and guidance of the GBT scheduling staff, and the provision of additional observation time to do these calibrations, is greatly appreciated. The Green Bank Observatory is a facility of the National Science Foundation operated under cooperative agreement by Associated Universities, Inc.

The guidance and support provided by Tim Robishaw, in setting up the Spider scan observations and providing details on determining the Mueller matrix, is acknowledged with gratitude. His input has been crucial for the observations and analysis presented in this paper.

We thank the anonymous referee for the thoughtful, thorough and constructive feedback that has provided valuable insights and improved the quality and comprehensiveness of the paper.

Facility: GBT.

Software: GBTIDL, Excel Add-in Solver.

Appendix A
Calibration of Spectra

The standard process to calibrate spectra for the auto-correlation terms (*XX* and *YY*) using the calibration ND reference signal is

$$\mathrm{Spectrum}_{\mathrm{data}} = \mathrm{Spectrum}_{\mathrm{on-source}} - \mathrm{Spectrum}_{\mathrm{background}}\ (\text{or baseline}), \quad \text{(A1)}$$

$$\mathrm{Spectrum}_{\mathrm{cal}} = \mathrm{Spectrum}(\mathrm{ND}_{\mathrm{ON}}) - \mathrm{Spectrum}(\mathrm{ND}_{\mathrm{OFF}}), \quad \text{(A2)}$$

$$\mathrm{Spectrum}_{\mathrm{calibrated}} = \mathrm{Spectrum}_{\mathrm{data}} / \mathrm{Spectrum}_{\mathrm{cal}} \times \mathrm{calibration-constant}. \quad \text{(A3)}$$

The calibration constant, to calibrate the spectrum in Kelvin or Janskys, is dependent on the ND calibration temperature. For the GBT, T_{cal} values are predetermined from observations and stored in the header of the SDFITS file. The standard GBT calibration provides the same value for *XX*, *XY,* and *YX* and a different calibration value for *YY*. As described in Section 4.3,

all the analysis and results in this paper are based on using the YY $T_{\rm cal}$ value for all polarizations, as using the values provided in the SDFITS header for XX and YY result in larger Mueller matrix ΔG values. The new analysis code (Fallon 2022) can cater for either the different predetermined $T_{\rm cal}$ values per polarization (as done in the standard GBTIDL routines) or applying the same $T_{\rm cal}$ for all polarizations.

The cross-polarization XY and YX spectra require polar coordinates to derive the relative dispersive phase that the calibration signal is accumulating. This calibration removes the linear phase gradient resulting from the ND deflection from each individual pair of the original XY and YX spectra. This calibration procedure has been implemented previously (Heiles & Robishaw 2022),[8] but is not included in the standard routines available at the GBT.

The method used is a polar coordinate calibration per channel, given by[9,10]

$$r_{\rm data} = \sqrt{(XY_{\rm data})^2 + (YX_{\rm data})^2}, \tag{A4}$$

$$\theta_{\rm data} = \arctan(YX_{\rm data}, XY_{\rm data}), \tag{A5}$$

$$r_{\rm cal} = \sqrt{(XY_{\rm cal})^2 + (YX_{\rm cal})^2}, \tag{A6}$$

$$\theta_{\rm cal} = \arctan(YX_{\rm cal}, XY_{\rm cal}), \tag{A7}$$

where

$$XY_{\rm cal} = XY\,({\rm ND_{ON}}) - XY\,({\rm ND_{OFF}}),$$
$$YX_{\rm cal} = YX\,({\rm ND_{ON}}) - YX\,({\rm ND_{OFF}}),$$

and the calibrated outcome is

$$r_{\rm calibrated} = r_{\rm data} \,/\, r_{\rm cal}, \tag{A8}$$

$$\theta_{\rm calibrated} = \theta_{\rm data} - \theta_{\rm cal}, \tag{A9}$$

$$XY_{\rm calibrated} = r_{\rm calibrated} \times \cos(\theta_{\rm calibrated}) \times {\rm calibration-constant}, \tag{A10}$$

$$YX_{\rm calibrated} = r_{\rm calibrated} \times \sin(\theta_{\rm calibrated}) \times {\rm calibration-constant}. \tag{A11}$$

[8] https://astro.berkeley.edu/~heiles/

[9] The $XY_{\rm data}$ and $YX_{\rm data}$ spectra have have their appropriate background or baseline removed as per Equation (A1).

[10] Note use of the arctan(y, x) or arctan2(y, x) function is crucial as this returns a value in the range $-180°$ and 180°, versus the general arctan(*single-value*) function, which only returns a value in the range $-90°$ and 90°.

Appendix B
Mueller Matrix Equations

The sky rotation matrix is given by

$$\boldsymbol{M}_{\rm sky} = \begin{bmatrix} 1 & 0 & 0 & 0 \\ 0 & \cos(2\ {\rm P.A.}) & \sin(2\ {\rm P.A.}) & 0 \\ 0 & -\sin(2\ {\rm P.A.}) & \cos(2\ {\rm P.A.}) & 0 \\ 0 & 0 & 0 & 1 \end{bmatrix}. \tag{B1}$$

Dividing Equation (5) by $I_{\rm src}$ gives the source fractional Stokes parameters, and the rotated fractional source Stokes parameters can be written as

$$(Q/I)_{\rm src,rot} = \cos(2\ {\rm P.A.})\,(Q/I)_{\rm src} + \sin(2\ {\rm P.A.})\,(U/I)_{\rm src} \tag{B2}$$

$$(U/I)_{\rm src,rot} = \sin(2\ {\rm P.A.})\,(Q/I)_{\rm src} + \cos(2\ {\rm P.A.})\,(U/I)_{\rm src}. \tag{B3}$$

The Mueller matrix described by Heiles et al. (2001) and Heiles (2002) iswhere

1. $\Delta\ G$ is the relative calibration gain between the X and Y components of the feed;
2. ψ is the phase difference between the the calibration ND signal and the incoming radiation;
3. α is a measure of the voltage ratio of the polarization ellipse produced when the feed observes pure linear polarization;
4. ϵ is a measure of imperfection of the feed in producing nonorthogonal polarizations (false correlations) in the two correlated outputs (represents undesirable cross coupling between the two polarizations); and
5. ϕ is the phase angle at which the voltage coupling ϵ occurs. It works with ϵ to couple I with (Q, U, V).

$$\begin{bmatrix} 1 & [-2\epsilon\sin\phi\sin 2\alpha + (\Delta G/2)\cos 2\alpha] & 2\epsilon\cos\phi & [2\epsilon\sin\phi\cos 2\alpha + (\Delta G/2)\sin 2\alpha] \\ \Delta G/2 & \cos 2\alpha & 0 & \sin 2\alpha \\ 2\epsilon\cos(\phi+\psi) & \sin 2\alpha\sin\psi & \cos\psi & -\cos 2\alpha\sin\psi \\ 2\epsilon\sin(\phi+\psi) & -\sin 2\alpha\cos\psi & \sin\psi & \cos 2\alpha\cos\psi \end{bmatrix}, \tag{B4}$$

Noting that for the linearly polarized calibration sources $V_{\rm src} = 0$, and assuming that $I_{\rm obs} = I_{\rm src}$, dividing Equation (5) by $I_{\rm obs}$, and multiplying out the components gives

$$1 = 1 + [-2\epsilon\sin\phi\sin 2\alpha + (\Delta G/2)\cos 2\alpha](Q/I)_{\rm src,rot} + 2\epsilon\cos\phi\,(U/I)_{\rm src,rot} \tag{B5}$$

$$(Q/I)_{\rm obs} = \Delta G/2 + \cos 2\alpha\,(Q/I)_{\rm src,rot} \tag{B6}$$

$$(U/I)_{\rm obs} = 2\epsilon\cos(\phi+\psi) + \sin 2\alpha\sin\psi(Q/I)_{\rm src,rot} + \cos\psi\,(U/I)_{\rm src,rot} \tag{B7}$$

$$(V/I)_{\rm obs} = 2\epsilon\sin(\phi+\psi) - \sin 2\alpha\cos\psi(Q/I)_{\rm src,rot} + \sin\psi\,(U/I)_{\rm src,rot}. \tag{B8}$$

Appendix C
Lo-Cal ND Mueller Matrices

Table 2
GBT Mueller Matrices for Evenly Spaced *C*-band Frequencies, Calculated from Two Observations of 3C 138, and One Observation of B0529+075 using the Lo-Cal ND on 2021 November 27

4.300 *GHz* − *Lo*−*Cal ND*	5.900 *GHz* − *Lo*−*Cal ND*
$\begin{bmatrix} 1.0000 & 0.0443 & -0.0150 & 0.0015 \\ -0.0443 & -0.9977 & 0.0000 & -0.0678 \\ 0.0151 & 0.0059 & -0.9962 & -0.0865 \\ -0.0002 & -0.0675 & -0.0867 & 0.9939 \end{bmatrix}$	$\begin{bmatrix} 1.0000 & -0.0404 & -0.0070 & 0.0004 \\ 0.0404 & -1.0000 & 0.0000 & 0.0081 \\ 0.0070 & -0.0003 & -0.9992 & -0.0399 \\ 0.0003 & 0.0081 & -0.0399 & 0.9992 \end{bmatrix}$
4.700 *GHz* − *Lo*−*Cal ND*	6.300 *GHz* − *Lo*−*Cal ND*
$\begin{bmatrix} 1.0000 & -0.0154 & -0.0039 & 0.0015 \\ 0.0154 & -1.0000 & 0.0000 & -0.0081 \\ 0.0038 & 0.0006 & -0.9974 & -0.0715 \\ 0.0019 & -0.0081 & -0.0715 & 0.9974 \end{bmatrix}$	$\begin{bmatrix} 1.0000 & 0.0194 & -0.0150 & -0.0096 \\ -0.0198 & -0.9991 & 0.0000 & 0.0433 \\ 0.0155 & -0.0030 & -0.9976 & -0.0688 \\ -0.0077 & 0.0432 & -0.0688 & 0.9967 \end{bmatrix}$
5.100 *GHz* − *Lo*−*Cal ND*	6.700 *GHz* − *Lo*−*Cal ND*
$\begin{bmatrix} 1.0000 & -0.0065 & -0.0046 & -0.0023 \\ 0.0065 & -0.9999 & 0.0000 & 0.0147 \\ 0.0047 & -0.0011 & -0.9972 & -0.0748 \\ -0.0020 & 0.0147 & -0.0748 & 0.9971 \end{bmatrix}$	$\begin{bmatrix} 1.0000 & -0.0232 & 0.0088 & 0.0164 \\ 0.0231 & -1.0000 & 0.0000 & -0.0059 \\ -0.0094 & 0.0002 & -0.9993 & -0.0364 \\ 0.0162 & -0.0059 & -0.0364 & 0.9993 \end{bmatrix}$
5.500 *GHz* − *Lo*−*Cal ND*	7.100 *GHz* − *Lo*−*Cal ND*
$\begin{bmatrix} 1.0000 & 0.0058 & -0.0124 & -0.0015 \\ -0.0058 & -0.9999 & 0.0000 & 0.0143 \\ 0.0124 & -0.0011 & -0.9972 & -0.0749 \\ -0.0005 & 0.0143 & -0.0749 & 0.9971 \end{bmatrix}$	$\begin{bmatrix} 1.0000 & -0.0362 & -0.0077 & -0.0110 \\ 0.0358 & -0.9994 & 0.0000 & 0.0341 \\ 0.0083 & -0.0017 & -0.9987 & -0.0509 \\ -0.0118 & 0.0341 & -0.0510 & 0.9981 \end{bmatrix}$

Table 3
GBT Mueller Matrices for Specific Maser Frequencies, Calculated using Lo-Cal ND Observations of 3C 138 and B0529+075 on 2021 January 5, Two Observations of 3C 138 and One Observation of B0529+075 on 2021 November 27

4.765 *GHz* − *Lo*−*Cal ND*	6.033 *GHz* − *Lo*−*cal ND*
$\begin{bmatrix} 1.0000 & -0.0157 & -0.0036 & -0.0010 \\ 0.0157 & -1.0000 & 0.0000 & 0.0028 \\ 0.0037 & -0.0003 & -0.9959 & -0.0905 \\ -0.0007 & 0.0028 & -0.0905 & 0.9959 \end{bmatrix}$	$\begin{bmatrix} 1.0000 & -0.0496 & -0.0140 & -0.0200 \\ 0.0496 & -1.0000 & 0.0000 & 0.0000 \\ 0.0152 & 0.0000 & -0.9979 & -0.0645 \\ -0.0191 & 0.0000 & -0.0645 & 0.9979 \end{bmatrix}$
4.751 *GHz* − *Lo*−*Cal ND*	6.049 *GHz* − *Lo*−*Cal ND*
$\begin{bmatrix} 1.0000 & -0.0195 & -0.0016 & -0.0021 \\ 0.0195 & -1.0000 & 0.0000 & -0.0079 \\ 0.0017 & 0.0006 & -0.9967 & -0.0813 \\ -0.0018 & -0.0079 & -0.0813 & 0.9967 \end{bmatrix}$	$\begin{bmatrix} 1.0000 & -0.0331 & -0.0089 & -0.0111 \\ 0.0330 & -1.0000 & 0.0000 & 0.0048 \\ 0.0093 & -0.0002 & -0.9993 & -0.0362 \\ -0.0109 & 0.0048 & -0.0362 & 0.9993 \end{bmatrix}$
4.660 *GHz* − *Lo*−*Cal ND*	6.181 *GHz* − *Lo*−*Cal ND*
$\begin{bmatrix} 1.0000 & -0.0255 & 0.0142 & -0.0015 \\ 0.0255 & -1.0000 & 0.0000 & -0.0032 \\ -0.0141 & 0.0003 & -0.9963 & -0.0854 \\ -0.0026 & -0.0032 & -0.0854 & 0.9963 \end{bmatrix}$	$\begin{bmatrix} 1.0000 & -0.0427 & -0.0037 & -0.0019 \\ 0.0427 & -0.9999 & 0.0000 & -0.0117 \\ 0.0039 & 0.0016 & -0.9908 & -0.1357 \\ -0.0009 & -0.0116 & -0.1357 & 0.9907 \end{bmatrix}$
4.830 *GHz* − *Lo*−*Cal ND*	6.668 *GHz* − *Lo*−*Cal ND*
$\begin{bmatrix} 1.0000 & -0.0038 & -0.0028 & -0.0004 \\ 0.0038 & -1.0000 & 0.0000 & 0.0099 \\ 0.0028 & -0.0008 & -0.9967 & -0.0811 \\ -0.0002 & 0.0098 & -0.0811 & 0.9967 \end{bmatrix}$	$\begin{bmatrix} 1.0000 & 0.0070 & -0.0021 & 0.0035 \\ -0.0070 & -1.0000 & 0.0000 & 0.0036 \\ 0.0019 & -0.0003 & -0.9976 & -0.0696 \\ 0.0036 & 0.0036 & -0.0696 & 0.9976 \end{bmatrix}$

Note. Data quality issues resulted in poor fitting for the 6.033 and 6.181 GHz matrices so these results should be used with caution.

Table 4
GBT Mueller Matrices at 4.700 GHz for Observations with Different Calibration Noise Diodes

4.700 *GHz* − *Hi*−*Cal ND*	4.700 *GHz* − *Lo*−*Cal ND*
$\begin{bmatrix} 1.0000 & -0.0009 & 0.0020 & -0.0007 \\ 0.0009 & -1.0000 & 0.0000 & -0.0004 \\ -0.0019 & 0.0000 & -0.9946 & -0.1042 \\ -0.0009 & -0.0004 & -0.1042 & 0.9946 \end{bmatrix}$	$\begin{bmatrix} 1.0000 & -0.0154 & -0.0039 & 0.0015 \\ 0.0154 & -1.0000 & 0.0000 & -0.0081 \\ 0.0038 & 0.0006 & -0.9974 & -0.0715 \\ 0.0019 & -0.0081 & -0.0715 & 0.9974 \end{bmatrix}$

Note. Differences are apparent, in particular, in the m_{IQ} and m_{QI} terms that represent the relative calibration gain in the *X* and *Y* channels.

ORCID iDs

Paul Fallon https://orcid.org/0000-0002-4846-1741
Derck P. Smits https://orcid.org/0000-0003-3593-9707
Tapasi Ghosh https://orcid.org/0000-0003-4454-2875
Christopher J. Salter https://orcid.org/0000-0002-3168-8659
Pedro Salas https://orcid.org/0000-0001-8271-0572

References

Fallon, P. 2022, GBT Memo 306, Green Bank Observatory, https://library.nrao.edu/public/memos/gbt/GBT_306.pdf
Goddy, J., Masters, K., & Stark, D. 2020, AAS Meeting Abstracts, 235, 167
Heiles, C. 2002, in ASP Conf. Proc. 278, Single-Dish Radio Astronomy: Techniques and Applications (San Francisco, CA: ASP), 131
Heiles, C., Perillat, P., Nolan, M., et al. 2001, PASP, 113, 1274
Heiles, C., & Robishaw, T. 2022, All-Stokes Single Dish Data with the RHSTK_2021 Software Package, https://w.astro.berkeley.edu/~heiles/
Heiles, C., Robishaw, T., Troland, T., & Roshi, D.-A. 2003, GBT Commissioning Memo 23, Green Bank Observatory, https://library.nrao.edu/public/memos/gbt/GBTCM_023.pdf
IEEE 2018, IEEE Standard Definitions of Terms for Radio Wave Propagation, IEEE Std 211-2018, doi:10.1109/IEEESTD.2019.8657413
Liao, Y.-W., Chang, T.-C., Kuo, C.-Y., et al. 2016, ApJ, 833, 289
Prestage, R. M., Bloss, M., Brandt, J., et al. 2015, in 2015 URSI-USNC Radio Science Meeting (New York: IEEE), 4
Robishaw, T., & Heiles, C. 2006, GBT Memo 244, Green Bank Observatory, https://library.nrao.edu/public/memos/gbt/GBT_244.pdf
Robishaw, T., & Heiles, C. 2021, The WSPC Handbook of Astronomical Instrumentation (Singapore: World Scientific), 127